

18

Time-Dependent Density Functional Study on the Excitation Spectrum of Point Defects in Semiconductors

Adam Gali

18.1

Introduction

Density functional theory (DFT) has been proven to be extremely powerful method to study defects in solids. Nowadays, this is a standard tool to investigate their concentration in thermal equilibrium, their interaction with each other, their vibration modes or their hyperfine tensors [1–5]. All these properties are associated with the ground state of the defect. The success of the DFT calculations are based on the well-developed approximate (semi)local functionals [6–9] that made possible to study relatively large systems at moderate computational cost with a surprisingly good accuracy. We mention here that the commonly used (semi)local functionals suffer from the self-interaction error [7] which results in the underestimation of the band gap of semiconductors. Nevertheless, for many semiconductors the (semi) local DFT calculations could predict qualitatively well the adiabatic (thermal) ionization energies of defects [1]. However, in pathological cases (semi)local functionals could fail to describe the nature of the defect states correctly due to the self-interaction error. Recent studies have shown [10–14] that non-local hybrid functionals could improve the results at large extent, and could provide quantitatively good results for the thermal ionization energies of point defects [15]. The effect of hybrid functionals is discussed in detail in another chapter in this book. We claim that hybrid density functionals provide relatively accurate quasi-particle energies and states compared to (semi)local functionals but these quasi-particle energies are still within the mean field approximation. In order to calculate the excitation spectrum properly one must go beyond the mean field approximation. Time-dependent DFT (TD-DFT) goes beyond this approximation. TD-DFT method has been successfully applied recently to calculate the excitation spectrum of molecules and semiconductor nanocrystals [16]. In some earlier studies efforts have been made to address the excitation of defect states in solids by TD-DFT method where “solids” were modeled by extremely small finite clusters including 5–50 host atoms [17–21]. However, it is very questionable whether the electron

states associated with the defect in a solid are properly described in such small clusters, and no thorough study has been carried out so far even for a single defect to address this very important issue.

We note that TD-DFT excitation spectrum obtained by (semi)local functionals is reliable only for finite structures [16]. In a very recent study it has been shown that hybrid density functional in the TD-DFT kernel provides appropriate excitation spectrum for infinite semiconductors [22]. Here, we restrict ourselves into finite structures where both the local and non-local functionals can be consistently applied and validate the results for bulk systems. We study two representative defects in wide gap semiconductors: nitrogen-vacancy (NV) center in diamond and divacancy in silicon carbide (SiC). A common behavior of these defects is that they produce characteristic transition in the photoluminescence (PL) spectrum. We briefly summarize the known properties of these defects below.

18.1.1

Nitrogen-Vacancy Center in Diamond

Nitrogen-vacancy center in diamond has attracted a lot of attention in recent years, since it has been detected at a single defect level [23, 24] and provides a quantum bit for quantum computing applications [25–30]. Besides providing a single photon source for quantum cryptography [31, 32], the NV center is also a promising candidate as an optically coupled quantum register for scalable quantum information processing, such as quantum communication [33] and distributed quantum computation [34]. In addition, it has been recently demonstrated that proximal nuclear spins can be coherently controlled via hyperfine interaction [35] and used as quantum memory with an extremely long coherence time [36].

The electronic structure of the NV center in diamond has been discussed in detail in a recent paper [37]. The NV center was found many years ago in diamond [38]. The model of the NV center consists of a substitutional nitrogen atom near a vacancy in diamond [38–42] as Figure 18.1a shows. The NV center has a strong optical transition with a zero phonon line (ZPL) at 1.945 eV (637 nm) accompanied by a vibronic band at higher energy in absorption with the largest intensity at about 2.20 eV and lower energy in emission (see also Figure 18.4). Detailed analysis of the ZPL revealed that the center has trigonal, C_{3v} symmetry [39]. Previous *ab initio* calculation clearly supported the negatively charged NV defect for 1.945 eV ZPL center [43–45] as was originally proposed by Loubser and van Wyk [40]. In the NV defect three carbon atoms have sp^3 dangling bonds near the vacancy (with three back bonds in the lattice) and nitrogen atom has also three back bonds with one dangling bond pointing to the vacant site. Since nitrogen has five valence electrons the negatively charged NV defect has altogether six electrons around the vacancy. One can use the defect-molecule picture [46] together with group theory to find the canonical orbitals of this system. According to this analysis there are two fully symmetric one-electron states (a_1) and one doubly degenerate e state which should be occupied by six electrons [44]. It was found that the two a_1 states is deeper in energy than the e state. As a consequence, four electrons occupy the a_1 states and two

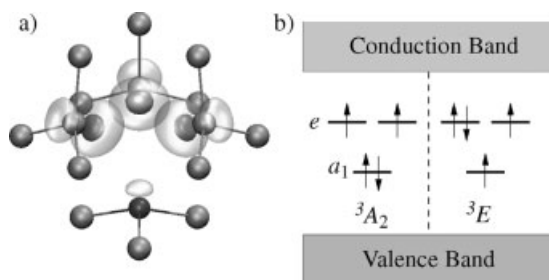


Figure 18.1 (online color at: www.pss-b.com) (a) The structure of N-V⁻ center in diamond; only first- and second-neighbor C (cyan spheres) and N (blue sphere) atoms to the vacant site are shown. The yellow and red lobes

are contours of the calculated spin-density. (b) Schematic diagram of the defect states in the gap and their occupation in the 3A_2 (ground) and 3E (excited) states.

electrons remain for the e state. Our calculated one-electron levels obtained by *ab initio* supercell (sc) calculations are shown in Figure 18.2.

As can be seen in Figure 18.2, the natural choice is to put the two remaining electrons parallel to the e level forming an $S = 1$ state (in analog to satisfy the Hund-rule for the p-orbitals of the isolated group IV elements in the periodic table). In the C_{3v} point group this total wave function has 3A_2 symmetry, where $3 = 2S + 1$ with $S = 1$. In our special case, we chose the $M_S = 1$, so both electrons are spin-up electrons on the e level. As can be seen, again in Figure 18.2, the lowest a_1 level is relatively deep in the valence band, so it seems to be a good approximation to assume that it does not contribute to the excitation process, and we do not consider it further. However, the next a_1 level in the gap is not very far from the e level. If one electron is excited from

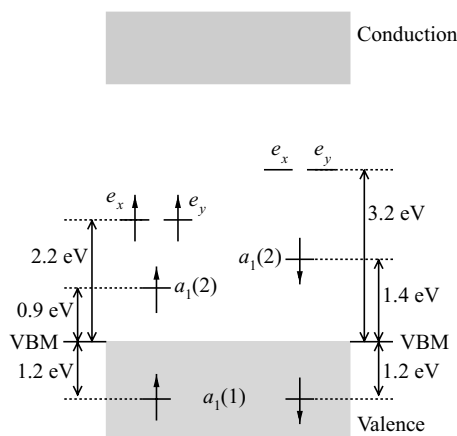


Figure 18.2 (online color at: www.pss-b.com) The calculated one-electron levels with respect to the valence band maximum in the ground state of the NV defect. The results obtained in a 512-atom supercell by applying the DFT within LDA functional in Ref. [44].

the this a_1 level into the e level then one will arrive at 3E state (see Figure 18.1b). The 3E is a doubly degenerate many-electron state, so it comprises two orthogonal many-electron states with the same eigenenergy. Both of them can be described by a single Slater-determinant: if the electron from a_1 level is promoted to e_x then the symmetry of the resulted many-electron state will be E_x , if it is promoted to e_y then the resulted many-electron state will be E_y . Thus, Figure 18.1b shows one of the true $M_S=1$ eigenstates of the excited state under C_{3v} symmetry (see Ref. [44] and references therein).

The only allowed transition is ${}^3A_2 \rightarrow {}^3E$ in the first order. Thus, the excitation of this system may be explained by promoting an electron from the a_1 single particle state to the e state resulting in the 3E excited state. This is certainly a simplified picture since the excited electron feels the presence of the hole left behind as a result of the Coulomb interaction between them, so they cannot be treated separately. Correspondingly, the wave function in the excited state, which should describe the motion of the correlated electron-hole pair, is *principally* not given by a simple product of electron and hole wave functions but requires a more general representation to account for energetic and spatial correlation between the two particles. Thus, we examine the excitation of NV center by TD-DFT theory which is able to address this complex phenomena. Before turning to the results we introduce another defect under consideration.

18.1.2

Divacancy in Silicon Carbide

Divacancies are common defects in semiconductors with consisting of neighbor isolated vacancies. The divacancy has been recently identified in hexagonal SiC polytypes [4]. The defect possesses C_{3v} symmetry in cubic SiC and also at on-axis configurations in hexagonal polytypes. The silicon vacancy part of the defect (C_{1-3} atoms) introduces three carbon dangling bonds while the carbon vacancy part of the defect (Si_{1-3} atoms) contributes with three silicon dangling bonds (see Figure 18.3). Again, group theory analysis revealed us [47] that the six dangling bonds will build two a_1 and two e defect levels in C_{3v} symmetry. Six electrons can occupy these states. According to our *ab initio* sc calculations [47] the two a_1 levels are lowest in energy and then the doubly degenerate e levels follow them in the hierarchy. Four electrons will occupy the a_1 states and the two remaining electron will occupy the degenerate e level. Again, by following the Hund-rule the natural choice is to place the electrons with parallel spins. Indeed, the ground state of the neutral divacancy is a high spin $S=1$ state [4, 47]

A PL spectrum of about 1.0 eV is associated with this defect which can be also detected at low temperature infrared absorption [48]. The nature of the excitation is not well-understood. The position of the defect levels may reveal the possible excitation mechanism of the defect. The two doubly degenerate e defect levels occur in the fundamental band gap [47]. In the ground state, only the lowest e level is occupied by parallel spin-electrons. Two a_1 defect levels are in the valence band where the highest a_1 state is resonant with the valence band edge according to our *ab initio* sc

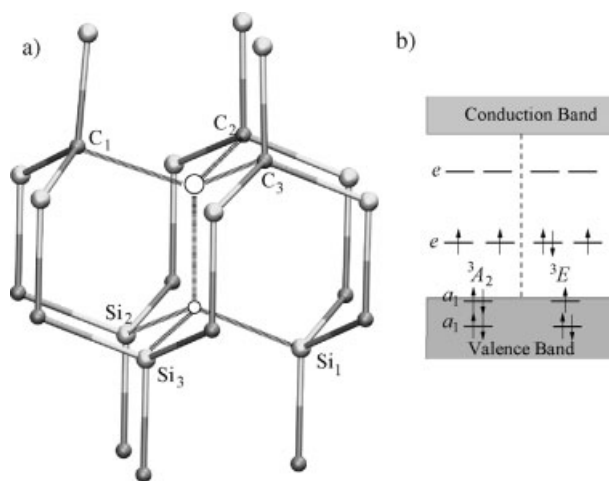


Figure 18.3 (online color at: www.pss-b.com) (a) The optimized geometry of the divacancy in the ground state. Cyan and yellow balls represent C and Si atoms, respectively. The open

circles depict the vacant sites. (b) Schematic diagram about the defect states in crystalline environment in the 3A_2 ground and 3E excited states.

calculations [47]. One possible model to explain the excitation is to promote an electron from the resonant a_1 state to the lowest e level in the fundamental gap [47] (Figure 18.3b). This will result in $^3A_2 \rightarrow ^3E$ excitation. The sharp excitation between a resonant state and a defect state in the fundamental gap is a well-known process in semiconductors, e.g., similar process takes place for the isolated vacancy in diamond [49]. Other excitations may also occur for divacancy in SiC, for instance, between the e defect levels in the gap. We examine the lowest excitation energies of divacancy by TD-DFT calculations.

18.2

Method

18.2.1

Model, Geometry, and Electronic Structure

We embed the defects into a nanocrystal that contains 147 host crystal atoms and 100 hydrogen atoms for termination. The results are strictly valid for these nanocrystals but we discuss whether the obtained results could be valid in crystalline environment. We applied PBE [9] functional to optimize the geometry while the excitation spectrum is calculated both by the semi-local PBE and non-local hybrid PBE0 functionals. In PBE0 functional the Hartree–Fock exchange is mixed at 25% extent into PBE functional [50]. The optimization of the geometry has been done with numerical atomic basis set for diamond nanocrystal at double ζ polarized

(DZP) level which provided good results in scs compared to plane wave calculations [44]. We used the SIESTA code for this purpose [51]. Troullier–Martins pseudopotentials have been applied to model the effect of nuclei together with the core electrons in SIESTA calculations [52]. We used the relatively computationally expensive VASP code with plane wave basis set [53, 54] to study the divacancy in SiC. In the VASP calculations, we use a plane wave basis set of 420 eV (~ 30 Ry) which is highly convergent with the applied projected augmentation wave (PAW) projectors for carbon, hydrogen, and silicon atoms [55, 56]. In the VASP calculations we applied the appropriate symmetry, and the energy of the ground state and the excited states are calculated by setting the appropriate occupation of the defect states in the gap as explained below. In the geometry optimization calculations, all the atoms were allowed to relax until the forces were below 0.01 eV/Å. In VASP code it is possible to set the occupation number of single particle states. This may be used to study the geometry change upon electronic excitation [12, 44]. In this scheme the excited state is described by promoting an electron from an occupied Kohn–Sham defect level to an unoccupied Kohn–Sham defect level of the ground state with allowing the nuclei to relax to find the optimum geometry with the charge density obtained from this fixed occupation of orbitals. This method is called *constrained* DFT briefly. The constrained DFT method is a computationally cheap method to find the ZPL transition energy within the Franck–Condon approximation as shown in Figure 18.4. In our experience this methodology *under special circumstances* provides reliable results regarding the *relaxation energy* due to electronic excitation [12] which is the Stokes-shift shown in Figure 18.4. The constrained DFT method may provide reliable results for the Stokes-shift upon the following conditions:

- 1) The excited state can be well-described by a single Slater-determinant and the symmetry of the ground and excited states are different with avoiding possible hybridization of states.
- 2) The nature of the excited and ground states is similar; for instance, they are originated from similar well-localized defect states.

As we show below we considered such defects here that can fulfill these criteria. Nevertheless, this statement cannot be proven by DFT based methods alone. We studied the nature of excitation by TD-DFT method that is capable of studying the above mentioned criteria. Next, we summarize the TD-DFT theory in nutshell with focusing on the approximations that make possible to use this method *in practice*.

18.2.2

Time-Dependent Density Functional Theory with Practical Approximations

In the TD-DFT within the Kohn–Sham formalism the system subject to a TD external potential:

$$\hat{v}_{\text{ext}}(\mathbf{r}, t) = \hat{v}_{\text{stat}}(\mathbf{r}) + \hat{v}_t(\mathbf{r})f(t), \quad (18.1)$$

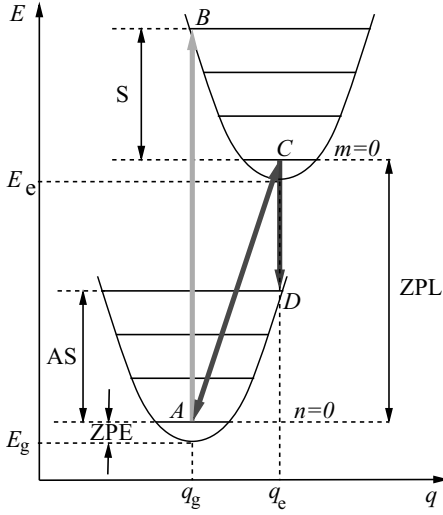


Figure 18.4 (online color at: www.pss-b.com) The energy (E) vs. configuration coordinate (q) diagram for the excitation process of a defect in the Franck–Condon approximation: E_g and E_e are the minima in the quasi-parabolic potential energy surfaces of the defect in the ground and excited states, respectively, and q_g and q_e are the corresponding coordinates. ZPE is the zero point energy (indicated only for the ground state). The energy ladders show the phonon energies with the phonon ground states at $n=0$

(ground state of the defect) and $m=0$ (excited state). At elevated temperatures the high-energy phonon states can be occupied by inducing transition $A \rightarrow B$ (vertical absorption, green arrow) and $C \rightarrow D$ (vertical emission, red arrow). Transition $A \leftrightarrow C$ corresponds to the zero-phonon line (ZPL, blue double arrow) both in absorption and emission. The energy of the Stokes-shift (S) and anti-Stokes-shift (AS) are also shown.

is mapped onto a effective one-particle (non-interacting) system (e.g., Refs. [57, 58]):

$$i\hbar \frac{\partial \varphi_i(\mathbf{r}, t)}{\partial t} = \hat{H}_{\text{eff}}(t) \varphi_i(\mathbf{r}, t), \quad (18.2)$$

where

$$\hat{H}_{\text{eff}}(t) = -\frac{1}{2} \nabla^2 + \hat{v}_{\text{ext}}(\mathbf{r}, t) + \int d^3 \mathbf{r}' \frac{\rho(\mathbf{r}', t)}{|\mathbf{r} - \mathbf{r}'|} + \hat{v}_{\text{xc}}[\rho](\mathbf{r}, t). \quad (18.3)$$

Here $\hat{v}_{\text{ext}}(\mathbf{r}, t)$ is the external potential, $\int d^3 \mathbf{r}' (\rho(\mathbf{r}', t)/|\mathbf{r} - \mathbf{r}'|)$ the Hartree term, and $\hat{v}_{\text{xc}}[\rho](\mathbf{r}, t)$ is the functional derivative of the TD exchange-correlation functional with respect to the TD density.

In the usual adiabatic approximation memory effects are neglected, i.e., $\hat{v}_{\text{xc}}[\rho](\mathbf{r}, t)$ is approximated as: $\hat{v}_{\text{xc}}[\rho](\mathbf{r}, t) = \hat{v}_{\text{xc}}(\rho(\mathbf{r}, t))$. This approximation is proven to be very successful in many cases and easy to implement. By using Eq. (18.2), one can propagate the wave function in real time and calculate the full spectrum of the system driven by Eqs. (18.1–18.3).

In many cases the excitation can be taken as a perturbing potential where the density response ($\rho^{(1)}(\mathbf{r}, t)$) is proportional to the perturbing potential (i.e., linear response theory):

$$\rho^{(1)}(\mathbf{r}, t) = \int d^3\mathbf{r}' dt' \chi(t, t', \mathbf{r}, \mathbf{r}') \hat{v}_i(\mathbf{r}') f(t'), \quad (18.4)$$

where $\chi(t, t', \mathbf{r}, \mathbf{r}')$ is the full response function. It can be shown that the density response in the Kohn–Sham picture takes the following form (see Ref. [58]):

$$\begin{aligned} \rho^{(1)}(\mathbf{r}, t) = & \int d^3\mathbf{r}' dt' \chi_{\text{KS}}(t, t', \mathbf{r}, \mathbf{r}') \\ & \times \left[\hat{v}_i(\mathbf{r}') f(t') + \int d^3\mathbf{r}'' \frac{\rho^{(1)}(\mathbf{r}'', t')}{|\mathbf{r}' - \mathbf{r}''|} \right. \\ & \left. + \int d^3\mathbf{r}'' \frac{\delta^2 E_{\text{xc}}}{\delta \rho(\mathbf{r}') \delta \rho(\mathbf{r}'')} \rho(\mathbf{r}'', t') \right], \end{aligned} \quad (18.5)$$

where $\chi_{\text{KS}}(t, t', \mathbf{r}, \mathbf{r}')$ is just the response function built from Kohn–Sham orbitals. Note that now the potential is not simply the TD part of Eq. (18.1), instead it also includes the Hartree-term and TD exchange-correlation potential, furthermore this equation has to be solved self-consistently since $\rho^{(1)}(\mathbf{r}, t)$ appears on both sides.

Now taking the Fourier transform of both sides ($f(\omega) = \int e^{i\omega t} f(t) dt$), we arrive at the equation:

$$\begin{aligned} \rho^{(1)}(\mathbf{r}, \omega) = & \int d^3\mathbf{r}' \chi_{\text{KS}}(\omega, \mathbf{r}, \mathbf{r}') \\ & \times \left[\hat{v}_i(\mathbf{r}') f(\omega) + \int d^3\mathbf{r}'' \frac{\rho^{(1)}(\mathbf{r}'', \omega)}{|\mathbf{r}' - \mathbf{r}''|} \right. \\ & \left. + \int d^3\mathbf{r}'' \frac{\delta^2 E_{\text{xc}}}{\delta \rho(\mathbf{r}') \delta \rho(\mathbf{r}'')} \rho(\mathbf{r}'', \omega) \right] \end{aligned} \quad (18.6)$$

In Fourier space the form of the response kernel is (where we also introduced spin dependence):

$$\begin{aligned} \chi_{\text{KS}, \sigma\sigma'}(\omega, \mathbf{r}, \mathbf{r}') = & \delta_{\sigma\sigma'} \sum_{i,a} \left[\frac{\varphi_{i\sigma}^*(\mathbf{r}) \varphi_{a\sigma}(\mathbf{r}) \varphi_{i\sigma'}(\mathbf{r}') \varphi_{a\sigma'}^*(\mathbf{r}')}{\omega - (\varepsilon_{a\sigma} - \varepsilon_{i\sigma}) + i0^+} \right. \\ & \left. - \frac{\varphi_{a\sigma}(\mathbf{r}) \varphi_{a\sigma}^*(\mathbf{r}) \varphi_{i\sigma'}^*(\mathbf{r}') \varphi_{a\sigma'}(\mathbf{r}')}{\omega + (\varepsilon_{a\sigma} - \varepsilon_{i\sigma}) + i0^+} \right]. \end{aligned} \quad (18.7)$$

In Eq. (18.7) $\varphi_{i\sigma}(\mathbf{r})$ s are ground-state Kohn–Sham orbitals. From now on, i, j and a, b indices denote occupied and virtual (unoccupied) orbitals, respectively. k, l, m, n indices stand for general orbitals.

In order to solve Eq. (18.6), let us parameterize the density response as follows:

$$\begin{aligned} \rho_{\sigma}^{(1)}(\mathbf{r}, \omega) = & \sum_{i,a,\sigma} [P_{ia\sigma}(\omega) \varphi_{a\sigma}^*(\mathbf{r}) \varphi_{i\sigma}(\mathbf{r}) \\ & + P_{a i \sigma}(\omega) \varphi_{a\sigma}(\mathbf{r}) \varphi_{i\sigma}^*(\mathbf{r})]. \end{aligned} \quad (18.8)$$

Using Eqs. (18.7) and (18.8) we arrive at the following coupled matrix equations for $P_{ia\sigma}(\omega)$ and $P_{a i \sigma}(\omega)$:

$$\begin{aligned} [\delta_{\sigma\tau} \delta_{ij} \delta_{ab} (\epsilon_{a\sigma} - \epsilon_{i\sigma} + \omega) + K_{ia\sigma, j b \tau}] P_{j b \tau} \\ + K_{ia\sigma, b j \tau} P_{b j \tau} = -(\hat{v}t)_{ia\sigma}, \end{aligned} \quad (18.9)$$

$$\begin{aligned} [\delta_{\sigma\tau} \delta_{ij} \delta_{ab} (\epsilon_{a\sigma} - \epsilon_{i\sigma} - \omega) + K_{a i \sigma, b j \tau}] P_{b j \tau} \\ + K_{a i \sigma, j b \tau} P_{j b \tau} = -(\hat{v}t)_{a i \sigma}, \end{aligned} \quad (18.10)$$

where we introduced the following short notation: $(\hat{v}t)_{ia\sigma} = \int d^3\mathbf{r} \varphi_{i\sigma}^*(\mathbf{r}) \hat{v}_t(\mathbf{r}) \varphi_{a\sigma}(\mathbf{r})$, and the K kernel:

$$\begin{aligned} K_{kl\sigma, mn\tau} = & \int d^3\mathbf{r} d^3\mathbf{r}' \varphi_{k\sigma}^*(\mathbf{r}) \varphi_{l\sigma}(\mathbf{r}) \\ & \times \left(\frac{1}{|\mathbf{r} - \mathbf{r}'|} + \frac{\delta^2 E_{xc}}{\delta \rho_{\sigma}(\mathbf{r}') \delta \rho_{\tau}(\mathbf{r}'')} \right) \varphi_{n\tau}^*(\mathbf{r}') \varphi_{m\tau}(\mathbf{r}''). \end{aligned} \quad (18.11)$$

Note that the kernel consists of two parts: the Hartree part is local in time (it causes the so-called *local field effects*), however the second part of the kernel is generally non-local both in space and time. In the adiabatic approximation derived above it is time independent but still space dependent. If the xc kernel is set to zero then this approximation is called the random phase approximation. Neglecting both terms in the kernel yield transitions between Kohn–Sham states.

Using $X_{ia\sigma} = P_{ia\sigma}(\omega)$, $Y_{ia\sigma} = P_{a i \sigma}(\omega)$, and $V_{ia\sigma} = (\hat{v}t)_{ia\sigma}$ we arrive at the following matrix equation:

$$\left[\begin{pmatrix} \mathbf{L} & \mathbf{M} \\ \mathbf{M}^* & \mathbf{L}^* \end{pmatrix} - \omega \begin{pmatrix} -1 & 0 \\ 0 & 1 \end{pmatrix} \right] \begin{pmatrix} \mathbf{X} \\ \mathbf{Y} \end{pmatrix} = -f(\omega) \begin{pmatrix} \mathbf{V} \\ \mathbf{V}^* \end{pmatrix}, \quad (18.12)$$

where

$$L_{ia\sigma, j b \tau} = \delta_{\sigma\tau} \delta_{ij} \delta_{ab} (\epsilon_{a\sigma} - \epsilon_{i\sigma}) + K_{ia\sigma, j b \tau}, \quad (18.13)$$

$$M_{ia\sigma, j b \tau} = K_{ia\sigma, b j \tau}. \quad (18.14)$$

In response theory, excitation energies are the poles of response function, thus by taking $f(\omega) = 0$ we find the following non-Hermitian eigenvalue problem:

$$\begin{pmatrix} \mathbf{L} & \mathbf{M} \\ \mathbf{M}^* & \mathbf{L}^* \end{pmatrix} \begin{pmatrix} \mathbf{X} \\ \mathbf{Y} \end{pmatrix} = \omega \begin{pmatrix} -1 & 0 \\ 0 & 1 \end{pmatrix} \begin{pmatrix} \mathbf{X} \\ \mathbf{Y} \end{pmatrix}, \quad (18.15)$$

This matrix equation is called Casida-equation [59]. We note that the term \mathbf{Y} may be neglected (the so-called anti-resonance between the occupied and unoccupied states) that leads to the so-called Tamm-Dancoff approximation. We keep further the anti-resonance term in our derivation. If the ground-state density originates from a restricted Kohn–Sham calculation ($\phi_{ia}(\mathbf{r}) = \phi_{i\beta}(\mathbf{r})$) then the size of the problem may be reduced by one half and a unitary transformation can help discriminate between singlet (s) and triplet (t) transitions:

$$u_{ia} = \frac{1}{\sqrt{2}}(P_{ia\alpha} + P_{ia\beta}), \quad v_{ia} = \frac{1}{\sqrt{2}}(P_{ia\alpha} - P_{ia\beta}). \quad (18.16)$$

It can be shown that if the orbitals can be chosen to be real (and that is true for finite structures) then the resulting matrices \mathbf{M}^p , \mathbf{L}^p will be also real where p labels either singlet (s) or triplet (t) excitations. The long expression for these matrices are given in the appendix of Ref. [60]. We note that these matrices contain the Hartree term and a modified expression for the xc term. In the case of hybrid functionals, the Hartree term is adjusted with respect to the case of (semi)local functionals. Now, we find the following matrix equation:

$$(\mathbf{M}^p - \mathbf{L}^p)(\mathbf{M}^p + \mathbf{L}^p)(\mathbf{X} + \mathbf{Y}) = \omega^2(\mathbf{X} + \mathbf{Y}). \quad (18.17)$$

If $\mathbf{M}^p - \mathbf{L}^p$ is positive definite, Eq. (18.17) can be transformed to a hermitian eigenvalue problem:

$$\begin{aligned} & (\mathbf{M}^p - \mathbf{L}^p)^{1/2}(\mathbf{M}^p + \mathbf{L}^p)(\mathbf{M}^p - \mathbf{L}^p)^{-1/2}(\mathbf{X} + \mathbf{Y})' \\ & = \omega^2(\mathbf{X} + \mathbf{Y})', \end{aligned} \quad (18.18)$$

with

$$(\mathbf{X} + \mathbf{Y})' = (\mathbf{M}^p - \mathbf{L}^p)^{-1/2}(\mathbf{X} + \mathbf{Y}). \quad (18.19)$$

Clearly, in order to obtain excitation energies, these matrices have to be build and the eigenvalue problem has to be solved. This is done using an iterative subspace method in Turbomole package [61]. We note that we obtain the transition energies in the frequency domain with this method which makes possible to restrict the calculations to the lowest excitation energies and to analyze the states contributing to the given excitation. This is a clear advantage over the time domain algorithms of TD-DFT where always the full spectrum is calculated and the analysis of the nature of transitions is not straightforward.

We applied the Turbomole package to carry out the TD-DFT calculations [61]. This is a cluster code with localized Gaussian basis sets that can utilize hybrid functional in the TD-DFT kernel. We applied an all-electron Gaussian DZP basis set for all the atoms in the system [62] at fixed coordinates supplied by Siesta or VASP DFT

calculations. We calculated the adiabatic TD-DFT spectrum both with spin-polarized (semi)local DFT-PBE and non-local PBE0 functionals within the linear response theory and beyond the Tamm-Dancoff approximation. We particularly focused on the lowest excitation energies that may be manifested in the low temperature absorption and PL spectra.

18.3

Results and Discussion

18.3.1

Nitrogen-Vacancy Center in Diamond

In nanodiamond the gap opens up only slightly by about 0.1 eV even in our relatively small nanodiamond with a diameter of about 1 nm. Recently, we have found [63] that nanodiamond exhibits low-lying Rydberg states which results in only small change between the highest occupied molecular orbital (HOMO)–lowest unoccupied molecular orbital (LUMO) gap of nanodiamonds and the band gap of bulk diamond. This will have a serious consequence on the TD-DFT spectrum as we will show below.

We started with the geometry optimization of the negatively charged NV center by SIESTA DFT-PBE calculations using spin-polarization and without symmetry restriction. The defect automatically arrived at the $S=1$ state and retained the C_{3v} symmetry. It may be worthy to compare the relative positions of the defect states obtained in nanodiamond (labeled as “nd”) and supercell (labeled as “sc”) DFT-PBE calculations.

Two defect levels appear in the HOMO–LUMO gap: the a_1 and e levels like in the sc calculations. By comparing the PBE single particle Kohn–Sham levels obtained in the sc and nanodiamond (columns 2 and 3 in Table 18.1), we observe that the relative positions of the defect levels are very similar including the spin-polarization between a_1^{α} and a_1^{β} states or the energy difference between a_1 and e states within the same spin-channel. This implies that the defect levels are “fixed” relative to each other and do not change significantly by confining the crystalline states. In our sc calculations we found [44] that these defect states are strongly localized around the core of the defect, in other words, they “split” from the extended crystalline states that are not effected heavily due to quantum confinement. One may hope that the results obtained in the nanodiamond model may be relevant for crystalline environment as the excitation may occur between the localized defect states.

Next, we may check the quasi-particle shift due to non-local functionals or by G0W0 correction [64, 65]. In the case of sc calculations, we used the *screened* hybrid HSE06 functional with $\omega = 0.20$ 1/Å screening parameter [66, 67] which provided nice agreement with the experimental band gap of diamond and excitation energies of the NV center [12]. For instance, we obtained the experimental vertical energy of absorption (2.20 eV) very accurately by using constrained DFT calculation and Δ SCF procedure. In the case of nanodiamond we use unscreened hybrid PBE0 which gave us very accurate absorption spectra for tiny nanodiamonds [63]. We believe that the

Table 18.1 The relative positions of defect levels of NV center in the ground state in eV where α and β label the spin-up and -down channels, respectively. The PBE and HSE06 supercell (sc) calculations have been carried out in 512-atom sc yielding accurate excitation energies with HSE06 functional (Ref. [12]) while G0W0 sc calculations have been made in 256-atom sc with about 0.15 eV larger excitation energies together with BSE than the experimental values (Ref. [64]). “nd” labels the results obtained in our nanodiamond. a_1^α , a_1^β , and e^α states are occupied while e^β is unoccupied in the ground state. LUMO is a Rydberg state in nanodiamond. The values in the parentheses are the relative quasi-particle corrections defined as the following: in column HSE06 sc this is the difference between column HSE06 sc and PBE sc carried out with the same

size of sc (but allowing relaxation with the two methods as explained in Ref. [12]); in column G0W0 sc the reference PBE values are taken from the same geometry and sc in Ref. [64]; in column PBE0 nd this is the energy difference between column PBE0 nd and PBE nd carried out in the same nanodiamond and with the same geometry. Lowest excitation energy (E_{exc}) is calculated by Δ SCF method for PBE sc and HSE06 sc methods, while with G0W0 + BSE method for G0W0 sc and TD-DFT for PBE nd and PBE0 nd. Exciton binding energy (E_x) is defined as an energy difference between the calculated excitation energy and the quasi-particle energy difference between the corresponding states in TD-DFT methods while BSE provides this value on the top of G0W0 sc calculation.

levels	PBE sc	PBE nd	HSE06 sc	G0W0 sc	PBE0 nd
$a_1^\beta - a_1^\alpha$	0.56	0.58	1.04 (0.48)	0.6 (0.2)	1.22 (0.64)
$e^\alpha - a_1^\alpha$	1.17	1.28	1.23 (0.06)	1.2 (0.1)	1.37 (0.09)
$e^\beta - a_1^\alpha$	2.45	2.44	4.00 (1.55)	3.3 (1.1)	4.67 (2.23)
$e^\beta - a_1^\beta$	1.89	1.84	2.96 (1.07)	2.7 (0.9)	3.45 (1.61)
LUMO- e^α		1.57			3.46
E_{exc}	1.91	1.57	2.21	2.32	2.20
E_x		0.0	0.75	0.30	1.25

unscreened hybrid functionals are more realistic for relatively small nanoclusters and molecules where the electron system cannot effectively screen the Coulomb potential like in an infinite crystal. By comparing the “HSE06 sc” and “PBE0 nd” columns we found that the quasi-particle shifts between occupied levels are very similar being but a bit (0.16 eV) larger for “PBE0 nd.” However, there is a larger difference between the relative positions of the unoccupied e^β and the occupied states with the two methods. The quasi-particle shift for the unoccupied state is larger with the unscreened PBE0 functional which may be a natural consequence of the larger Fock-exchange term in the Hamiltonian. The G0W0 sc calculations have been carried out at the Γ -point in 256-atom sc [64] which may not be fully convergent for the single particle states but still it is worthwhile to compare the G0W0 quasi-particle levels with those obtained by hybrid functionals. The spin-polarization of a_1 state (~ 0.2 eV) is not enhanced such a large amount like with hybrid functionals (0.5–0.6 eV) after the quasi-particle correction. Interestingly, the quasi-particle shift difference relative to a_1^α is also larger for HSE06 sc than for G0W0 sc, thus the quasi-particle shift difference for ($e^\beta - a_1^\alpha$) will be similar.

Now, we turn to the investigation of the excitation energies. In the case of the TD-DFT calculation with PBE kernel we arrived at a very low value of 1.57 eV. According to

our analysis the $e^{\alpha} \rightarrow \text{LUMO}$ transition is responsible for this absorption peak. As can be inferred in Table 18.1 the energy of LUMO is indeed close to the energy of the highest occupied spin-up defect level e^{α} . Apparently, this transition cannot occur in crystalline environment. The next lowest transition energy is about 1.88 eV which is close to the lowest excitation energy calculated in the sc by ΔSCF method (PBE sc column in Table 18.1). However, this excitation peak arises in only 39% from $a_1^{\beta} \rightarrow e^{\beta}$ transition but 57% from $e^{\alpha} \rightarrow \text{LUMO} + 1$ transition. This indicates that the TD-DFT spectrum at PBE level cannot describe the nature of transition occurring in bulk diamond due to the low-lying empty Rydberg state of nanodiamond. We note that the calculated “exciton binding energy” of the lowest excitation is practically zero which is typical for TD-DFT spectrum with (semi)local functionals in the kernel. The situation for the TD-DFT calculation with PBE0 in the kernel is different. In PBE0 the LUMO level is about the same energy distance from the e^{α} state as the energy difference between a_1^{β} and e^{β} levels. The lowest excitation energy is 2.20 eV which is dominated by $a_1^{\beta} \rightarrow e^{\beta}$ transition as much as 92%. While the energy difference between these single particle states was large (3.45 eV) due to the large quasi-particle shift between these states relative to their PBE values (1.61 eV) the large excitonic effect (1.25 eV) could compensate this effect with providing an excitation energy (2.20 eV) which is very close to the experimental value. This number is also close to the values resulted from HSE06 sc and G0W0 + BSE (Bethe-Salpeter equation) sc calculations (Table 18.1). We believe that it is not fortuitous coincidence. HSE06 sc gave less quasi-particle shift than PBE nd and correspondingly the “exciton binding energy” in HSE06 sc is smaller than for PBE nd. In G0W0 + BSE sc calculation we found the smallest quasi-particle shift with again smaller “exciton binding energy.” The unscreened PBE0 functional may overshoot the “quasi-particle shifts” relative to the PBE values but the large excitonic effect compensate this resulting in reasonable values for the excitation energies. This implies that the calculated “exciton binding energies” of defects in nanocrystals cannot reveal the “exciton binding energies” of defects in the bulk counterpart but the calculated excitation energies may be accurate after careful choice of the model and inspection the nature of the transition. From this investigation we can also conclude for NV center in diamond that the lowest excitation is indeed described by promoting an electron from the a_1^{β} level to the e^{β} level that can support the constrained DFT method to calculate the Stokes-shift for the PL process applied in Refs. [12, 64]. We note here that this transition describes the absorption of the light with perpendicular polarization to the symmetry axis which transforms as E irreducible representation in C_{3v} point group. The parallel polarized light transforms as A_1 under C_{3v} point group. According to the selection rules E polarization will be allowed for ${}^3A_2 \rightarrow {}^3E$ transition in the first order while A_1 polarization is forbidden. Our finding is in line with this group theory analysis.

18.3.2

Divacancy in Silicon Carbide

In our previous DFT-LDA sc calculation, we observed that neutral divacancy introduces two doubly degenerate defect levels in the gap (see Figure 18.3). Beside

these states two a_1 level is associated with the dangling bonds according to the group theory [47]. The highest a_1 level is resonant with the valence band edge with ~ 0.3 eV below the valence band top. In the ground state the lowest e level in the gap is occupied by two electrons. In spin-polarized calculation this e level splits by about 0.5 eV while the empty e level does not split practically.

In the DFT-PBE cluster calculation the “band gap” of SiC opens up with several eV compared to their bulk counterpart [68]. We note that we do not observe low-lying Rydberg states for SiC nanocluster like in diamond nanoclusters thus no such complications can occur in the analysis of the excitation spectrum of divacancy in SiC nanocrystals as for NV center in nanodiamond. The quantum confinement of crystalline states makes the resonant a_1 state visible that is localized strongly on the carbon dangling bonds. Because this a_1 state does not mix with the crystalline states, therefore the spin-polarization of this a_1 state is significant (~ 0.7 eV) in contrast to the case of DFT-LDA sc calculation. The a_1^β state will push up the lowest empty e^β state by about 0.5 eV, thus the energy difference between the lowest and highest e^β states will be about 0.5 eV smaller than in sc calculation. It is important to notice that the relative position of the a_1^α and e^α states agree those in sc calculation within 0.1 eV. This may indicate that the localized resonant state also sticks with the other localized defect states and splits from the crystalline environment. In the C_{3v} symmetry we determined the excitation energies with different light polarizations. As expected, the excitation with E polarization is lowest in energy which allows to couple the 3A_2 ground state and the 3E excited state. Indeed, in this case the excitation between a_1^β and lowest e^β states is dominant, however, there is a non-negligible contribution (13%) from the lowest and highest e^α states. The calculated absorption energy is 1.15 eV that is close to the measured ZPL transition of 1.0 eV. For the excitation with E polarization we obtained 1.43 eV which occurs between the lower and higher e^α defect states. We note that the corresponding “exciton binding energy” is zero as we found already for NV center in diamond.

Next, we studied this excitation by applying PBE0 hybrid functional in the TD-DFT kernel. The relative position between the occupied a_1^α and e^α defect levels remains about the same (~ 0.7 – 0.8 eV). However, the energy differences between the lower occupied and higher empty e^α states and between the occupied a_1^β and empty e^β states are increased by about 1.7–1.8 eV. This quasi-particle shift is a natural consequence of the Fock-operator in the hybrid functional which opens the gap between the occupied and unoccupied states. Again, we calculated the lowest excitation energies with A_1 and E polarizations. The excitation energy with E polarization is 1.18 eV which almost coincides with the value obtained by the (semi) local PBE in the TD-DFT kernel. The basic difference between the two transitions that in TD-DFT with PBE0 in the kernel the transition is dominated (over 95%) by promoting the electron from the single particle a_1^β defect level to the lowest e^β level. The relative quasi-particle shift of about 1.8 eV was largely compensated by the excitonic effect of about 1.0 eV. Interestingly, the next excitation energy of 1.85 eV is due to the transition between the a_1^β state and the higher e^β state. The “exciton binding energy” of this process is again ~ 1.0 eV. The following excitation energy of ~ 2.35 eV is caused by transitions of E , A_1 polarizations between the lower occupied

and higher empty e^α defect states where the resulting “exciton binding energy” is smaller (~ 0.8 eV).

We calculated the Stokes-shift due to electronic excitation by constrained DFT method. First, we studied the lowest excitation energy for which the transition between a_1^β and the lower e^β states is the dominant process resulting in the 3E excited state as shown in Figure 18.3b. We set this occupation for the defect states and restricted the geometry optimization within C_{3v} symmetry. The calculated Stokes-shift is 0.075 eV. Because the e^β state is half occupied Jahn-Teller distortion may occur. By allowing C_{1h} geometry optimization we obtained a slightly deeper energy than for C_{3v} symmetry. The final value for this Stokes-shift is 0.12 eV. By combining the absorption energy (1.18 eV) and the Stokes-shift we arrived at 1.06 eV for the ZPL line which is very close to the experimental value found in bulk SiC. We found that the deviation from the C_{3v} symmetry is tiny, still it is not exactly C_{3v} symmetry. Thus, the strict selection rule of E polarization of light in the emission process may be relaxed and A_1 polarization may be slightly allowed. The situation is different for the second lowest excitation process. In that case the a_1^β electron is excited to the higher e^β state. That higher e^β state is localized on the Si dangling bonds that can overlap and interact with each other. The Jahn-Teller distortion for this excited state is much stronger (~ 0.2 eV) than for the previous process (~ 0.04 eV) with resulting in a large Stokes-shift of 0.46 eV. Combining this value with the calculated absorption energy (1.85 eV) one arrives at 1.39 eV ZPL energy. Here, the C_{3v} symmetry is considerably lowered to C_{1h} where the Si_2 and Si_3 atoms are bended to each other (see Figure 18.3a). Thus, both polarizations should be allowed for this PL process.

These results are strictly valid for the SiC nanocrystal. As both the resonant a_1 state and the lowest e state remains “fixed” going from crystalline environment to small nanocrystal one may hope that the calculated TD-DFT excitation energy is valid for the defect in bulk SiC. Indeed, the calculated lowest excitation energy in SiC nanocrystal is close to the experimental data recorded in bulk SiC. By assuming that the transition from the resonant defect state is the strongest to the lower e level we may claim that we could identify the physical process in the PL center associated with the divacancy [48]. Our calculations revealed that other type of excitations may also occur for divacancy. In crystalline environment the detection of the resonances occurring in SiC nanocrystals may be not feasible due to competing processes. For instance, from the sea of the valence electrons lying in the continuous valence band one can excite an electron to the lower e level instead of the resonant excitation between the a_1 level and the higher e level where the latter process is clearly observable in our calculation due to the discrete energy spectrum of the relatively small SiC nanocrystal.

By comparing the excitation and other properties of NV center in diamond and divacancy in SiC one can list the similarities of the two systems:

- 1) The defect exhibits $S = 1$ high spin-state with C_{3v} symmetry.
- 2) The lowest excitation is due to ${}^3A_2 \rightarrow {}^3E$ transition.
- 3) The spin-density is localized close to the core of the defect.

Nevertheless, one can find also differences between the two systems:

- 1) Two highly localized well-separated defect states play the dominant role in the excitation of the NV center in diamond while one of the defect states is resonant with the valence band for the divacancy in SiC.
- 2) NV center has strict C_{3v} symmetry in the PL process while for divacancy in SiC it may be a bit lowered to C_{1h} symmetry.
- 3) NV center has a clear PL signal at room temperature while this has not yet been demonstrated by divacancy in SiC.
- 4) The spin-flip process in the PL process was already demonstrated for NV center in diamond while this has not been investigated in detail for divacancy in SiC, though electron paramagnetic resonance studies combined with photo-excitation indicate that similar process may occur for divacancy.

Further investigations are needed on divacancy in bulk SiC in order to explore the fine details of its excited states. One may say from the present study that divacancy in SiC might be an alternative for realizing the concept of solid state quantum bit.

18.4

Summary

We investigated the excitation spectrum of NV center in nanodiamond and divacancy in SiC nanocrystal. We found that TD-DFT method with PBE0 in the kernel could reproduce the experimental data observed in their bulk counterparts. We discussed the validity of these results by careful inspection of the model and its electronic structure. Our results imply that TD-DFT method with non-local DFT functional together with nanocrystal models may be applied for studying the excitation of defects in bulk crystals when the excitation occurs between well-localized defect states.

Acknowledgements

AG acknowledges the support from Hungarian OTKA under grant no. K-67886 and the János Bolyai program of the Hungarian Academy of Sciences.

References

- 1 de Walle, C.G.V. and Neugebauer, J. (2004) *J. Appl. Phys.*, **95** (8), 3851–3879.
- 2 Estreicher, S.K., Backlund, D., Gibbons, T.M., and Dočaj, A., *Model. Simul. Mater. Sci. Eng.*, **17** (8), 084006 (2009).
- 3 Blöchl, P.E. (2000) *Phys. Rev. B*, **62**, 6158.
- 4 Son, N.T., Carlsson, P., Hassan ul, J., Janzén, E., Umeda, T., Isoya, J., Gali, A., Bockstedte, M., Morishita, N., Ohshima, T., and Itoh, H. (2006) *Phys. Rev. Lett.*, **96**, 055501.
- 5 Umeda, T., Son, N.T., Isoya, J., Janzén, E., Ohshima, T., Morishita, N., Itoh, H., Gali, A., and Bockstedte, M. (2006) *Phys. Rev. Lett.*, **96**, 145501.

- 6 Ceperley, D.M. and Alder, B.J. (1980) *Phys. Rev. Lett.*, **45**, 566.
- 7 Perdew, J.P., and Zunger, A. (1981) *Phys. Rev. B*, **23**, 5048.
- 8 Perdew, J.P. and Wang, Y. (1992) *Phys. Rev. B*, **45** (23), 13244–13249.
- 9 Perdew, J.P., Burke, K., and Ernzerhof, M. (1996) *Phys. Rev. Lett.*, **77** (18), 3865–3868.
- 10 Deák, P., Gali, A., Sólyom, A., Buruzs, A., and Frauenheim, T. (2005) *J. Phys.: Condens. Matter*, **17** (22), S2141.
- 11 Oba, F., Togo, A., Tanaka, I., Paier, J., and Kresse, G. (2008) *Phys. Rev. B*, **77** (24), 245202.
- 12 Gali, A., Janzén, E., Deák, P., Kresse, G., and Kaxiras, E. (2009) *Phys. Rev. Lett.*, **103** (18), 186404.
- 13 Lyons, J.L., Janotti, A., and de Walle, C. G. V. (2009) *Appl. Phys. Lett.*, **95** (25), 252105.
- 14 Clark, S.J., Robertson, J., Lany, S., and Zunger, A. (2010) *Phys. Rev. B*, **81** (11), 115311.
- 15 Deák, P., Aradi, B., Frauenheim, T., Janzén, E., and Gali, A. (2010) *Phys. Rev. B*, **81** (15), 153203.
- 16 Onida, G., Reining, L., and Rubio, A. (2002) *Rev. Mod. Phys.*, **74** (2), 601–659.
- 17 Uchino, T., Takahashi, M., and Yoko, T. (2000) *Phys. Rev. Lett.*, **84** (7), 1475–1478.
- 18 Raghavachari, K., Ricci, D., and Pacchioni, G. (2002) *J. Chem. Phys.*, **116** (2), 825–831.
- 19 Zyubin, A.S., Mebel, A.M., and Lin, S.H. (2005) *J. Chem. Phys.*, **123** (4), 044701.
- 20 Zyubin, A.S., Mebel, A.M., Hayashi, M., Chang, H.C., and Lin, S.H. (2009) *J. Comput. Chem.*, **30** (1), 119–131.
- 21 Zyubin, A.S., Mebel, A.M., Hayashi, M., Chang, H.C., and Lin, S.H. (2009) *J. Phys. Chem. C*, **113** (24), 10432–10440.
- 22 Paier, J., Marsman, M., and Kresse, G. (2008) *Phys. Rev. B*, **78** (12), 121201.
- 23 Gruber, A., Drabenstedt, A., Tietz, C., Fleury, L., Wrachtrup, J., and Borczykowski, C. (1997) *Science*, **276**, 2012.
- 24 Drabenstedt, A., Fleury, L., Tietz, C., Jelezko, F., Kilin, S., Nizovtzev, A., and Wrachtrup, J. (1999) *Phys. Rev. B*, **60**, 11503.
- 25 Wrachtrup, J., Kilin, S.Y., and Nizotsev, A.P. (2001) *Opt. Spectrosc.*, **91**, 429.
- 26 Jelezko, F., Popa, I., Gruber, A., Tietz, C., Wrachtrup, J., Nizovtsev, A., and Kilin, S. (2002) *Appl. Phys. Lett.*, **81**, 2160.
- 27 Jelezko, F., Gaebel, T., Popa, I., Gruber, A., and Wrachtrup, J. (2004) *Phys. Rev. Lett.*, **92**, 076401.
- 28 Jelezko, F., Gaebel, T., Popa, I., Dunham, M., Gruber, A., and Wrachtrup, J. (2004) *Phys. Rev. Lett.*, **93**, 130501.
- 29 Epstein, R.J., Mendoza, F., Kato, Y.K., and Awschalom, D.D. (2005) *Nature Phys.*, **1**, 94.
- 30 Hanson, R., Mendosa, F.M., Epstein, R.J., and Awschalom, D.D. (2006) *Phys. Rev. Lett.*, **97**, 087601.
- 31 Brouri, R., Beveratos, A., Poizat, J.P., and Gragier, P. (2000) *Opt. Lett.*, **25**, 1294.
- 32 Beveratos, A., Brouri, R., Gacoin, T., Poizat, J.P., and Grangier, P. (2002) *Phys. Rev. A*, **64**, 061802R.
- 33 Childress, L., Taylor, J.M., Sørensen, A.S., and Lukin, M.D. (2006) *Phys. Rev. Lett.*, **96**, 070504.
- 34 Jiang, L., Hodges, J.S., Maze, J.R., Maurer, P., Taylor, J.M., Cory, D.G., Hemmer, P.R., Walsworth, R.L., Yacoby, A., Zibrov, A.S., and Lukin, M.D. (2009) *Science*, **326**, 267–272.
- 35 Childress, L., Gurudev Dutt, M.V., Taylor, J.M., Zibrov, A.S., Jelezko, F., Wrachtrup, J., Hemmer, P.R., and Lukin, M.D. (2006) *Science*, **314**, 281.
- 36 Gurudev Dutt, M.V., Childress, L., Jiang, L., Togan, E., Maze, J., Jelezko, F., Zibrov, A.S., Hemmer, P.R., and Lukin, M.D. (2007) *Science*, **316**, 312.
- 37 Manson, N.B., Harrison, J.P., and Sellars, M.J. (2006) *Phys. Rev. B*, **74**, 104303.
- 38 du Preez, L. (1965) Ph.D. dissertation, University of Witwatersrand, Johannesburg .
- 39 Davies, G. and Hamer, M.F. (1976) *Proc. R. Soc. Lond., A*, **348**, 285.
- 40 Loubser, J. H. N. and van Wyk, J.P. 1977) *Diamond Research (London)* Industrial

- Diamond Information Bureau, London, pp. 11–15.
- 41 Loubser, J. H. N. and van Wyk, J.A. (1978) *Rep. Prog. Phys.*, **41**, 1201.
 - 42 Collins, A.T. (1983) *J. Phys. C*, **16**, 2177.
 - 43 Goss, J.P., Jones, R., Breuer, S.J., Briddon, P.R., and Öberg, S. (1996) *Phys. Rev. Lett.*, **77**, 3041.
 - 44 Gali, A., Fyta, M., and Kaxiras, E. (2008) *Phys. Rev. B*, **77** (15), 155206.
 - 45 Larsson, J.A. and Delaney, P. (2008) *Phys. Rev. B*, **77** (16), 165201.
 - 46 Watts, R.K. (1977) *Point Defects in Crystals* Wiley-Interscience Publication, New York/London/Sydney/Toronto.
 - 47 Janzén, E., Gali, A., Henry, A., Ivanov, I.G., Magnusson, B., and Son, N.T. (2009), *Defects in SiC* Taylor & Francis Group, Boca Raton, FL, chap. 21, p. 615.
 - 48 Magnusson, B. and Janzén, E. (2005) *Mater. Sci. Forum*, **483–485**, 341.
 - 49 Lowther, J.E. (1993) *Phys. Rev. B*, **48** (16), 11592–11601 .
 - 50 Perdew, J.P., Ernzerhof, M., and Burke, K. (1996) *J. Chem. Phys.*, **105** (22), 9982–9985 .
 - 51 Sánchez-Portal, D., Ordejón, P., Artacho, E., and Soler, J.M. (1997) *Int. J. Quantum Chem.*, **65**, 543.
 - 52 Troullier, N. and Martins, J.L. (1991) *Phys. Rev. B*, **43**, 1993.
 - 53 Kresse, G. and Hafner, J. (1994) *Phys. Rev. B*, **49**, 14251.
 - 54 Kresse, G. and Furthmüller, J. (1996) *Phys. Rev. B*, **54**, 11169.
 - 55 Blöchl, P.E. (1994) *Phys. Rev. B*, **50**, 17953.
 - 56 Kresse, G. and Joubert, D. (1999) *Phys. Rev. B*, **59**, 1758.
 - 57 Runge, E. and Gross, E. K. U. (1984) *Phys. Rev. Lett.*, **52** (12), 997.
 - 58 Gross, E.K.U. and Kohn, W. (1990) *Adv. Quantum Chem.*, **21**, 255.
 - 59 Casida, M.E. (1995) *Recent Advances in Density Functional Theory* World Scientific, Singapore, p. 155.
 - 60 Bauernschmitt, R. and Ahlrichs, R. (1996) *Chem. Phys. Lett.*, **256** (4–5), 454– 464 .
 - 61 Ahlrichs, R., Bär, M., Häser, M., Horn, H., and Klumel, C. (1989) *Chem. Phys. Lett.*, **162** (Oct), 165– 169 .
 - 62 Schuchardt, K.L., Didier, B.T., Elsethagen, T., Sun, L., Gurumoorathi, V., Chase, J., Li, J., and Windus, T.L. (2007) *J. Chem. Inform. Model.*, **47**, 1045.
 - 63 Vörös, M. and Gali, A. (2009) *Phys. Rev. B*, **80** (16), 161411.
 - 64 Ma, Y., Rohlfing, M., and Gali, A. (2010) *Phys. Rev. B*, **81** (4), 041204.
 - 65 Hedin, L. and Lundqvist, S. (1969) in: *Solid State Physics*, (eds H. Ehrenreich, F. Seitz and D. Turnbull), Academic, New York.
 - 66 Heyd, J., Scuseria, G.E., and Ernzerhof, M. (2003) *J. Chem. Phys.*, **118** (18), 8207– 8215 .
 - 67 Krukau, A.V., Vydrov, O.A., Izmaylov, A.F., and Scuseria, G.E. (2006) *J. Chem. Phys.*, **125** (22), 224106.
 - 68 Vörös, M., Deák, P., Frauenheim, T., and Gali, A. (2010) *Appl. Phys. Lett.*, **96** (5), 051909.